PHYSICAL REVIEW D VOLUME 43, NUMBER 6 15 MARCH 1991

# Nonlinear wave solutions to the planar vacuum Einstein equations

Peter Anninos* and Joan Centrella
*Department of Physics and Atmospheric Science, Drexel University, Philadelphia, Pennsylvania 19104*

Richard A. Matzner
*Department of Physics and Center for Relativity, The University of Texas at Austin, Austin, Texas 78712*

(Received 4 September 1990)

We use the 3+1 split of spacetime and the York splitting into free and constrained variables to set up initial data and solve the vacuum Einstein equations in plane symmetry. We present numerical solutions for free data in the form of traveling waves in both the linear and nonlinear regimes. No evidence of nonlinear wave propagation is found and we demonstrate that for our class of metrics the nonlinearity lies in the "Coulomb" or nonradiative components of the Riemann curvature tensor.

## I. INTRODUCTION

For all the progress in recent years in finding solutions to the classical Einstein field equations, many basic issues remain unresolved. One of these areas is the basic nonlinear physics of the gravitational self-interaction. For example, what is the mechanism of nonlinear interactions between two waves? How do waves distort the background cosmological model through which they propagate? And do traveling waves steepen to form shocks or spread out through dispersion? These are some of the questions we address in this paper.

We have begun a program to study the simplified problem of one-dimensional (1D), i.e., one spatial dimension plus time, plane-symmetric solutions.[1-3] In particular, we study the initial-value construction and evolution of linear and nonlinear plane-symmetric gravitational waves in an expanding universe described by the Gowdy $T^3$ (Refs. 4–6) class of metrics. We write this metric in the 3+1 split as

$$ds^2 = -(\alpha^2 - \phi^4\beta^2)dt^2 + 2\phi^4\beta\, dz\, dt + \phi^4(dx^2 + h^2 dy^2 + dz^2) , \tag{1.1}$$

where $\alpha, \beta, \phi, h$ are functions of $z$ and $t$ only. We use units in which the speed of light $c=1$. The metric variable $h$ describes transverse anisotropy, and $\phi$ is the conformal factor. The lapse function $\alpha$ and shift vector $\beta$ determine the evolution of the coordinate system off the initial spacelike slice. The system we consider is periodically identified in the spatial coordinate $z$. Thus all variables must be periodic with period equal to the identification length $L$. This metric is well suited to the study of plane gravitational waves.

Our approach uses a combination of analytic and numerical techniques. On the one hand, we carry out a perturbative treatment of the equations to second order. In addition, we construct a numerical code to solve for fully developed nonlinear solutions. We will not discuss this code here, but will refer the reader to companion papers[1-3] where we have presented our numerical techniques in detail along with some interesting solutions to the field equations. We have tested our code extensively against both exact and perturbative (first- and second-order) analytic solutions. The results of such tests, which may be found in Refs. 1, 2, and 3, indicate that our code is accurate, reliable, and robust enough to study highly nonlinear problems without the code breaking down. We will rely heavily on our code to generate solutions and help analyze our results.

## II. GRAVITATIONAL-WAVE QUANTITIES

To describe gravitational-wave phenomena, we have found it instructive to compute the Newman-Penrose scalars[7] and the Bel-Robinson superenergy tensor.[8] In this section we briefly describe these quantities and present more explicit forms for the metric (1.1) in the Appendix.

Newman and Penrose[7] introduced a formalism leading to a compact set of equations which characterize the ten independent components of the Riemann tensor in vacuum by five complex and scalars. These scalars are the following null tetrad components of the Riemann tensor:

$$\Psi_0 = R_{\alpha\beta\gamma\delta} k^\alpha m^\beta k^\gamma m^\delta , \tag{2.1}$$

$$\Psi_1 = R_{\alpha\beta\gamma\delta} k^\alpha l^\beta k^\gamma m^\delta , \tag{2.2}$$

$$\Psi_2 = \tfrac{1}{2} R_{\alpha\beta\gamma\delta} (k^\alpha l^\beta k^\gamma l^\delta - k^\alpha l^\beta m^\gamma \overline{m}^\delta) , \tag{2.3}$$

$$\Psi_3 = R_{\alpha\beta\gamma\delta} l^\alpha k^\beta l^\gamma \overline{m}^\delta , \tag{2.4}$$

$$\Psi_4 = R_{\alpha\beta\gamma\delta} l^\alpha \overline{m}^\beta l^\gamma \overline{m}^\delta , \tag{2.5}$$

where we denote the vectors making up the null tetrad basis as **k**, **l**, **m**, and $\overline{\mathbf{m}}$, and an overbar denotes complex conjugation. Lower-case Latin letters represent spatial indices and Greek letters denote four-dimensional spacetime indices. The vectors **m** and $\overline{\mathbf{m}}$ are obtained from a set of real orthogonal unit spacelike vectors $a_\mu$ and $b_\mu$ in the $x$-$y$ plane:

$$m_\mu=\frac{1}{\sqrt{2}}(a_\mu+ib_\mu)=\frac{1}{\sqrt{2}}[0,\phi^2,ih\phi^2,0] , \qquad (2.6)$$

$$\overline{m}_\mu=\frac{1}{\sqrt{2}}(a_\mu-ib_\mu)=\frac{1}{\sqrt{2}}[0,\phi^2,-ih\phi^2,0] . \qquad (2.7)$$

We define the vectors **l** and **k** by adding and subtracting a spacelike unit vector $r_\alpha$ (orthogonal to $a_\mu$ and $b_\mu$) and a unit timelike vector $n_\alpha$ normal to the time slices:

$$k_\alpha=\frac{1}{\sqrt{2}}(n_\alpha+r_\alpha)=\frac{1}{\sqrt{2}}[\beta\phi^2-\alpha,0,0,\phi^2] , \qquad (2.8)$$

$$l_\alpha=\frac{1}{\sqrt{2}}(n_\alpha-r_\alpha)=\frac{1}{\sqrt{2}}[-\beta\phi^2-\alpha,0,0,-\phi^2] . \qquad (2.9)$$

For the metric (1.1), $\Psi_0$, $\Psi_2$, and $\Psi_4$ are the only nonvanishing scalars. These scalars were given the following physical interpretation by Szekeres:[9] $\Psi_0$ and $\Psi_4$ represent transverse waves propagating along the $-r^\alpha$ (negative $z$ axis) and the $+r^\alpha$ (positive $z$ axis) directions, respectively, while the $\Psi_2$ term is the "Coulomb" component dominated by nonradiative time-dependent gravitational fields.

The Bel-Robinson "superenergy" has been suggested[8,10,11] as a useful quantity in tracking gravitational-wave disturbances. The superenergy tensor is defined as[11]

$$T_{\alpha\beta\gamma\delta}=\tfrac{1}{2}(R_{\alpha\mu\gamma\nu}R_{\beta}{}^{\mu}{}_{\delta}{}^{\nu}+{}^*R_{\alpha\mu\gamma\nu}{}^*R_{\beta}{}^{\mu}{}_{\delta}{}^{\nu}) , \qquad (2.10)$$

where

$${}^*R_{\alpha\beta\gamma\delta}=\tfrac{1}{2}R^{\mu\nu}{}_{\gamma\delta}\epsilon_{\mu\nu\alpha\beta} . \qquad (2.11)$$

It has been demonstrated[10-12] that this tensor has properties remarkably analogous to those of the electromagnetic-field tensor, allowing a definition of a kind of gravitational field "energy density" via $T_{\alpha\beta\gamma\delta}$. The superenergy density scalar $E_s$ associated with a spacelike hypersurface with unit normal $n^\alpha$ is[10]

$$E_s=T_{\alpha\beta\gamma\delta}n^\alpha n^\beta n^\gamma n^\delta . \qquad (2.12)$$

Although $E_s$ depends on the slicing of spacetime, it is non-negative on any spacelike hypersurface and its van-

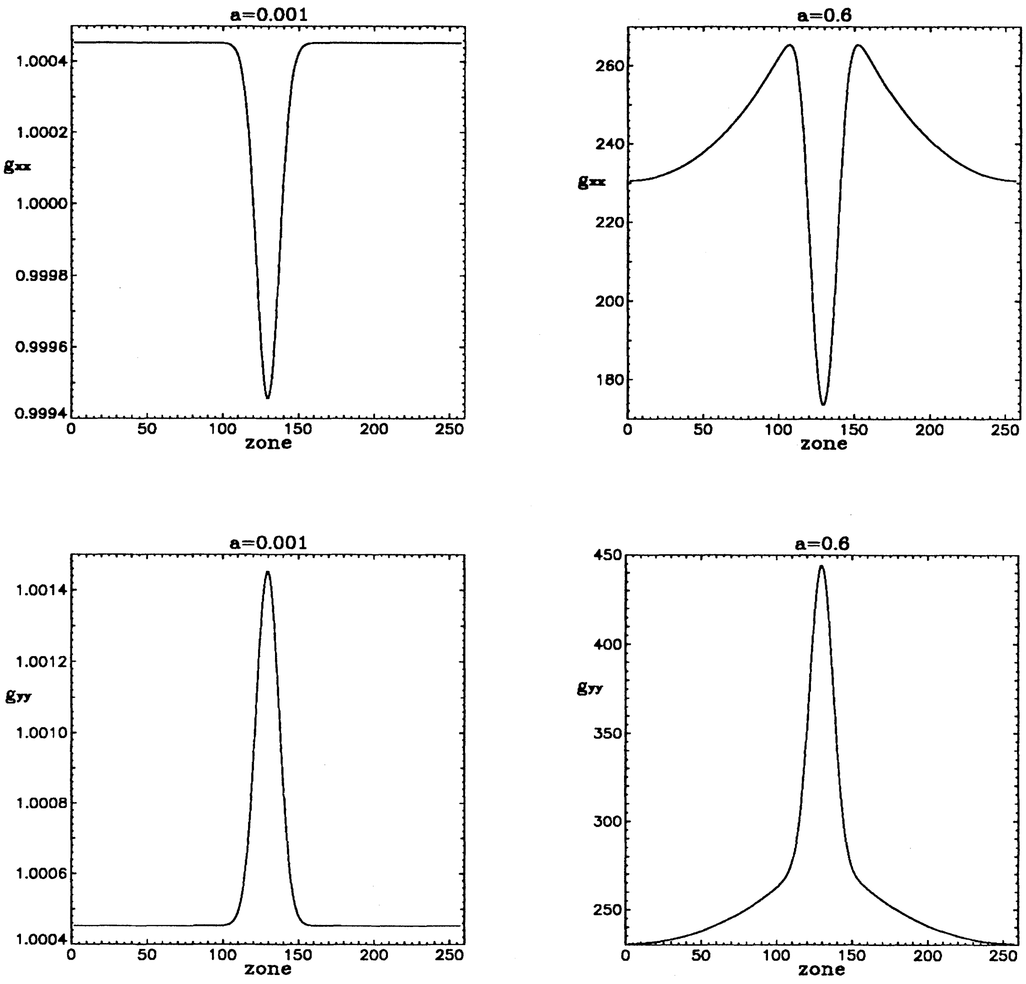

FIG. 1. Initial-data solutions for the metric components $g_{xx}$ and $g_{yy}$ for small- ($a=0.001$) and large- ($a=0.6$) amplitude high-frequency ($L=0.05L_H$) wave perturbations of the Kasner model with free data of the form of a Gaussian packet defined by (4.1).

ishing implies flat spacetime. We can define a corresponding Poynting vector[10,11]

$$p^{\mu}=T_{\alpha\beta\gamma\delta}n^{\beta}n^{\gamma}n^{\delta}\gamma^{\alpha\mu} , \qquad (2.13)$$

which, together with the superenergy, may be used to define a local velocity field

$$v^{\mu}=\frac{p^{\mu}}{E_s} . \qquad (2.14)$$

## III. TRAVELING WAVES AT SECOND PERTURBATIVE ORDER

In Ref. 3 we establish an analytical framework describing linear high-frequency waves by a perturbation expansion about the spatially homogeneous solutions to the vacuum field equations. These background solutions are the spatially homogeneous Kasner metrics and are usually expressed in terms of proper time $T$ as

$$ds^2=-dT^2+T^{2p_1}+T^{2p_2}dy^2+T^{2p_3}dz^2 , \qquad (3.1)$$

where the Einstein equations restrict the constant parameters $p_1$, $p_2$, and $p_3$:

$$p_1+p_2+p_3=1 , \qquad (3.2a)$$

$$p_1^2+p_2^2+p_3^2=1 . \qquad (3.2b)$$

These solutions fit our metric form (1.1) with the choices $\alpha=1$ and $\beta=0$ plus the restriction that $p_1=p_3$. There are two such axisymmetric Kasner models: (1) $p_1=\frac{2}{3}$, $p_2=-\frac{1}{3}$ (axisymmetric vacuum expanding cosmology) and (2) $p_1=0$, $p_2=1$ (flat space in expanding Milne-type coordinates).

In this paper we deal mostly with the axisymmetric Kasner model. For this case the perturbation expansion is

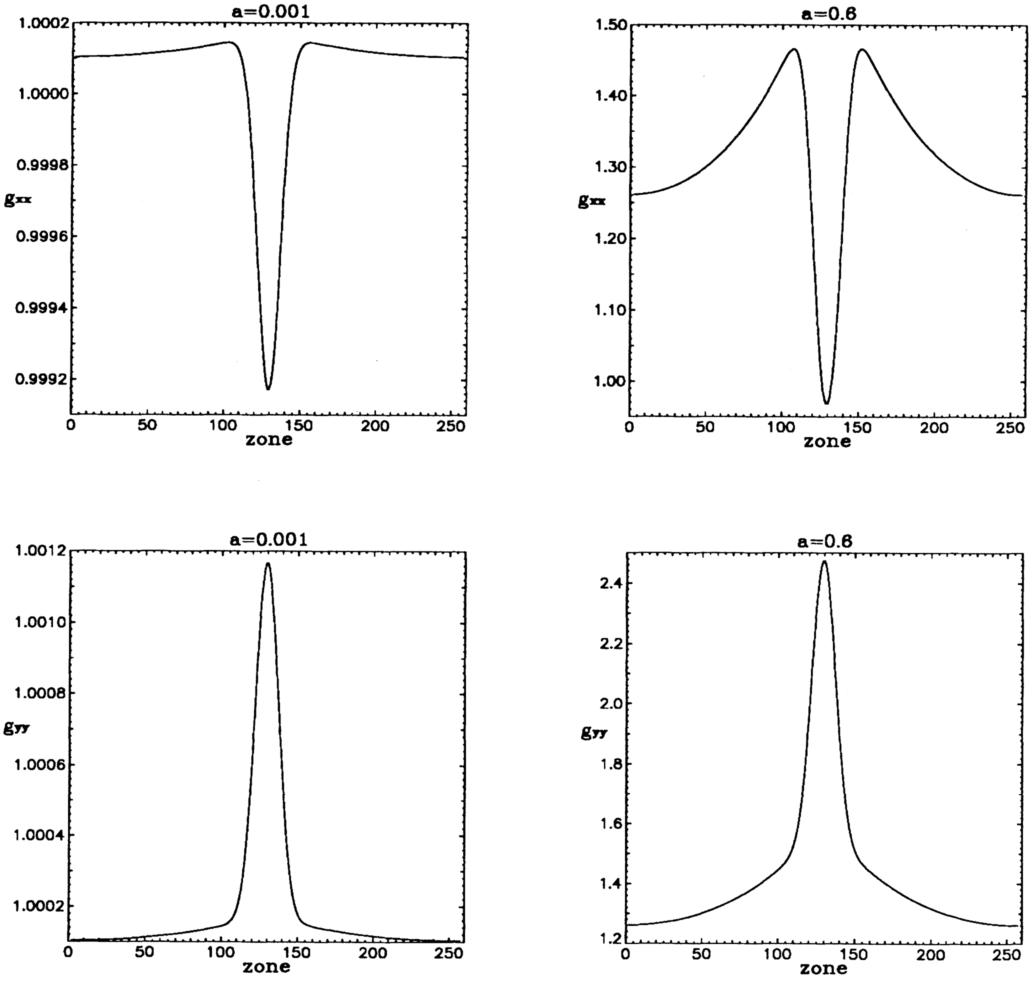

FIG. 2. Same as Fig. 1 except for moderate-frequency ($L=L_H$) perturbations.

$$h=\frac{1}{t}(1+h_1+h_2)\ , \tag{3.3a}$$

$$\phi=t^{1/3}(1+\phi_1+\phi_2)\ , \tag{3.3b}$$

$$\hat{\eta}=-t(1+\hat{\eta}_1+\hat{\eta}_2)\ , \tag{3.3c}$$

$$\hat{A}=-\frac{t}{3}(1+\hat{A}_1+\hat{A}_2)\ , \tag{3.3d}$$

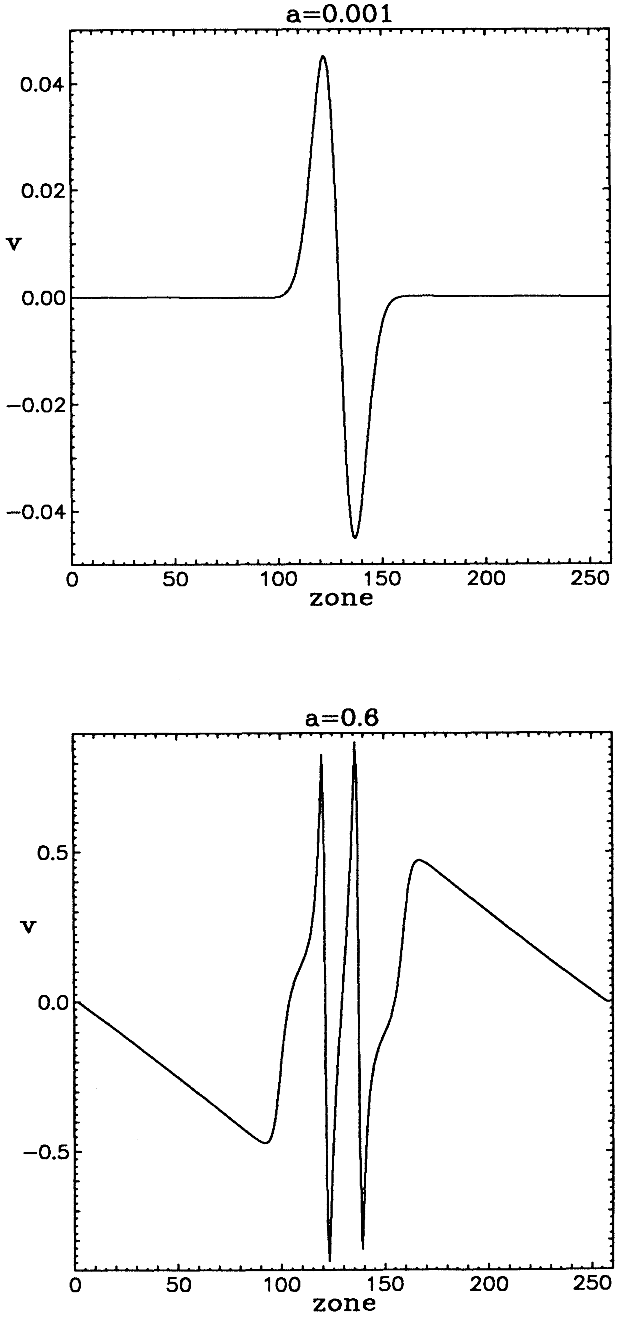

FIG. 3. The Bel-Robinson velocity for the case of moderate-frequency ($L=L_H$) perturbations of the Kasner model shown in Fig. 2. We present plots for initial data with small ($a=0.001$) and large- ($a=0.6$) amplitude perturbations in the form of Gaussian packets defined by (4.1).

$$K=-\frac{1}{t}(1+K_1+K_2)\ , \tag{3.3e}$$

$$\beta=0+\beta_1+\beta_2\ , \tag{3.3f}$$

and

$$\alpha=1+\alpha_1+\alpha_2\ . \tag{3.3g}$$

The meaning of this expansion is that quantities with a subscript 1 are first order in some smallness parameter $\epsilon$, while quantities with a subscript 2 are second order. The zeroth-order quantities are solutions to the field equation for the metric (3.1) with $p_1=\frac{2}{3}$ and $p_2=-\frac{1}{3}$. Here $K$ is the trace of the extrinsic curvature, and $\hat{\eta}$ and $\hat{A}$ are the conformally transformed trace-free parts of the extrinsic curvature.[1-3] In what follows we set $K_1=K_2=\dot{K}_1=\dot{K}_2=0$, which means that the spacelike slices in both the background and perturbed spacetimes have the same mean curvature.

The limit of high frequency is defined by $\lambda/L_H \ll 1$, where $\lambda$ is the perturbation wavelength and $L_H$ is the horizon size. Since the horizon size is proportional to $t^{1/3}$ (Ref. 3) in the Kasner model, the high-frequency limit is $kt^{1/3} \gg 1$ for perturbations with wave number $k$. In Ref. 3, we found (among other solutions) the following first-order Kasner solutions in this high-frequency regime:

$$h_1=\frac{BD}{2(3kt^{1/3})^{1/2}}[\sin(kz+3kt^{1/3}) -\sin(kz-3kt^{1/3})] \tag{3.4}$$

and

$$\hat{\eta}_1=-\frac{BD}{2\sqrt{3}}(kt^{1/3})^{1/2}[\cos(kz+3kt^{1/3}) +\cos(kz-3kt^{1/3})]\ , \tag{3.5}$$

where $BD$ is the perturbation amplitude. These results describe two equal strength nondispersive waves traveling in opposite directions with the same coordinate speed equal to unity, so that a slowly time varying ($t^{\pm 1/6}$) standing-wave pattern is obtained.

Next, we proceed to investigate the higher-order corrections, by solving the second-order equations for the Kasner perturbations $h_2$ and $\hat{\eta}_2$ in the high-frequency limit. We write these equations as

$$\dot{h}_2=\beta_1 h_1'-\frac{1}{t}(\hat{\eta}_2+\tfrac{5}{2}h_1\hat{\eta}_1) \tag{3.6}$$

and

$$\dot{\hat{\eta}}_2=\beta_1\hat{\eta}_1'+\frac{3}{2t}\hat{\eta}_1^2-\frac{1}{t^{1/3}}\left[h_2''-\frac{3}{2}h_1h_1''-\frac{(h_1')^2}{2}\right]\ , \tag{3.7}$$

where we have kept only the lowest-order terms in the frequency expansion. We can combine these equations to obtain a single second-order partial differential equation for $h_2$:

$$\ddot{h}_2+\frac{\dot{h}_2}{t}-\frac{h_2''}{t^{4/3}}=\frac{\hat{\eta}_1^2}{t^2}+\frac{1}{t^{4/3}}\left[h_1h_1''-\frac{(h_1')^2}{2}\right]-\frac{2\beta_1\hat{\eta}_1'}{t}+\dot{\beta}_1h_1' \ . \tag{3.8}$$

The right-hand side of Eq. (3.8) is known in terms of the first-order solutions presented in Ref. 3. Substituting those solutions into (3.8) results in

$$\ddot{h}_2+\frac{\dot{h}_2}{t}-\frac{h_2''}{t^{4/3}}=\frac{(BD)^2k}{3t^{5/3}}\cos(6kt^{1/3}) \ . \tag{3.9}$$

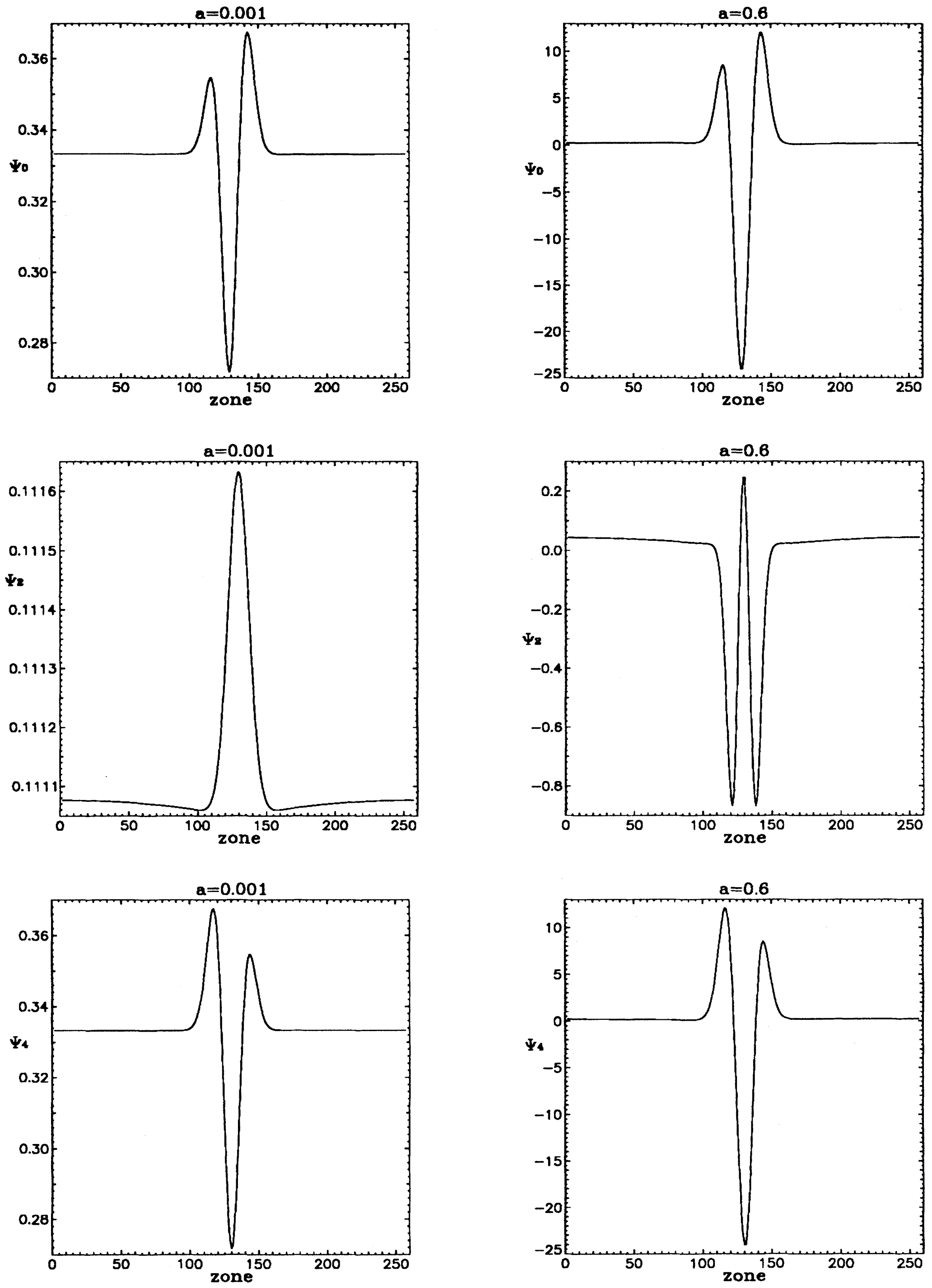

FIG. 4. Profiles of the Newman-Penrose scalars $\Psi_0$, $\Psi_2$, and $\Psi_4$ in the initial data for the same linear and nonlinear moderate-frequency cases shown in Figs. 2 and 3.

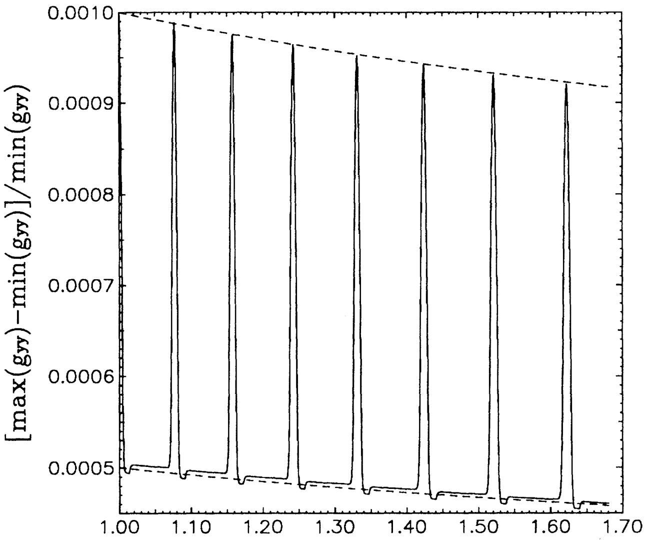

FIG. 5. Evolution of (5.1) plotted in the solid line is used to characterize high-frequency $L=0.05L_H$ traveling pulses with $a=0.001$ for the free data (4.1). The dashed lines give the decay of the wave amplitude predicted by our first-order high-frequency perturbation solution for the Kasner model (Ref. 3).

Equation (3.9) is simplified somewhat by introducing the variable substitution $\tilde{t}=3t^{1/3}$ to rewrite it as

$$\frac{\partial^2 h_2}{\partial \tilde{t}^2}+\frac{1}{\tilde{t}}\frac{\partial h_2}{\partial \tilde{t}}-\frac{\partial^2 h_2}{\partial z^2}=\frac{(BD)^2 k}{\tilde{t}}\cos(2k\tilde{t}) \ . \qquad (3.10)$$

Note that the source terms in (3.10) are not functions of the coordinate $z$. This allows us to assume a spatially constant solution for $h_2$ with $\partial^2 h_2/\partial z^2=0$. The resulting equation has the solution

$$h_2-h_{20}=c_1\ln\frac{\tilde{t}}{\tilde{t}_0}+\frac{B^2D^2}{2}\int_{u_0}^{u}\frac{\sin u}{u}du \ , \qquad (3.11)$$

where $u=2k\tilde{t}$ and $h_{20}$ and $c_1$ are integration constants defined by $h_{20}=h_2(\tilde{t}=\tilde{t}_0)$ and

$$c_1=\tilde{t}_0\dot{h}_{20}-\frac{B^2D^2}{2}\sin 2k\tilde{t}_0 \ , \qquad (3.12)$$

with $\dot{h}_{20}=\dot{h}_2(\tilde{t}=\tilde{t}_0)$. The integral in these equations is the sine integral denoted by

$$\mathrm{Si}(u)=\int_0^u\frac{\sin u}{u}du \ , \qquad (3.13)$$

which may be approximated by[13]

$$\mathrm{Si}(u)\approx\frac{\pi}{2}-\frac{\cos u}{u} \ , \qquad (3.14)$$

in the high-frequency limit ($k\tilde{t}\gg 1$). Applying this limit to the integral equation (3.11), we have

$$h_2=c_1\ln\frac{t^{1/3}}{t_0^{1/3}}-c_2\frac{\cos 6kt^{1/3}}{6kt^{1/3}}+c_3 \ , \qquad (3.15)$$

where $c_1$ is defined in Eq. (3.12) and

$$c_2=\frac{B^2D^2}{2} \ , \qquad (3.16)$$

$$c_3=\frac{B^2D^2}{2}\frac{\cos 6kt_0^{1/3}}{6kt_0^{1/3}}+h_{20} \ , \qquad (3.17)$$

We note that the first- and second-order equations for the flat-space [$p_1=0$ and $p_2=1$ in (3.1)] perturbations have similar solutions for $h$. The only difference is that $3kt^{1/3}$ is replaced with $t$ in Eqs. (3.4) and (3.15)–(3.17). The second-order solution (3.15) is not a traveling wave. Instead, it produces oscillatory behavior in time of the "background" spacetime with frequencies equal to the harmonics of the first-order standing-wave solution, in addition to providing a monotonic increase in its expansion rate. To second perturbative order we find no evidence of nonlinear *wave* interactions. In the remaining sections of the paper we use numerical techniques to explore the solution space of the field equations. Our findings support the analytic results.

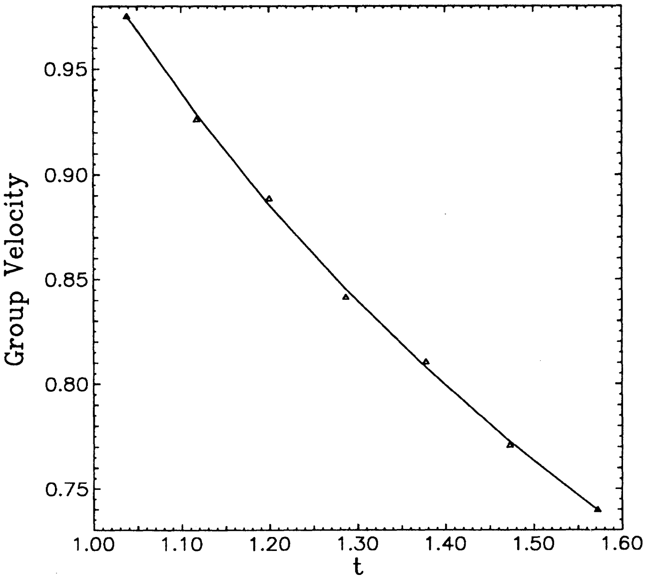

FIG. 6. Group velocity for high-frequency pulses moving across the grid in the Kasner model for the case shown in Fig. 5. The analytical solution $t^{-2/3}$ is given by the solid line. Triangles denote code solutions which are obtained by tracking the world line of a single wave peak.

## IV. INITIAL-VALUE PULSE WAVE SOLUTIONS

Here we present solutions to the initial value equations in the form of localized wave pulses. To assure linearization stability[1,2] we choose our free data in the form

$$h=\sigma\hat{\eta}=1+ae^{-(z-z_0)^2/(2w^2)}, \tag{4.1}$$

where $z_0=L/2$ locates the pulse peak at the grid center, $w=0.03$ defines the pulse half-width as 3% of our grid length, $a$ is the variable pulse amplitude, and $\sigma$ denotes the background spacetime: $\sigma=+1$ for flat space and $\sigma=-1$ for the axisymmetric expanding Kasner model. In this section and for the remainder of this paper, we will consider perturbations of the Kasner background. Our simulations of flat-space perturbations proved similar in nature to the Kasner case. Note that Eq. (4.1) is not strictly compatible with periodic boundary conditions. However, the perturbation term drops exponentially and results in a value of $h$ and $\hat{\eta}$ at both grid edges that is sufficiently flat (vanishing first derivatives) and close to unity that periodicity is guaranteed for practical purposes in the numerical solutions.

In Figs. 1–4 we present our numerical solutions to the initial-wave equations for perturbations of the Kasner model. Solutions to the three-metric components $g_{xx}$ and $g_{yy}$ are displayed along with the Newman-Penrose scalars and the Bel-Robinson velocity in the parameter space of increasing perturbation amplitude $a$.

First, we consider solutions for the metric components $g_{xx}$ and $g_{yy}$ in the high-frequency ($L=0.05L_H$) and moderate-frequency ($L=L_H$) regimes. Figure 1 presents solutions to $g_{xx}$ and $g_{yy}$ in the high-frequency regime with perturbation amplitudes $a=0.001$ and 0.6. The small-amplitude case exhibits linear behavior in the sense that the constraint equations reproduce the sharp profile of the Gaussian packet used for our free data. However, the nonlinear case shows that the pulse perturbation distorts the background spacetime to the point in which per-

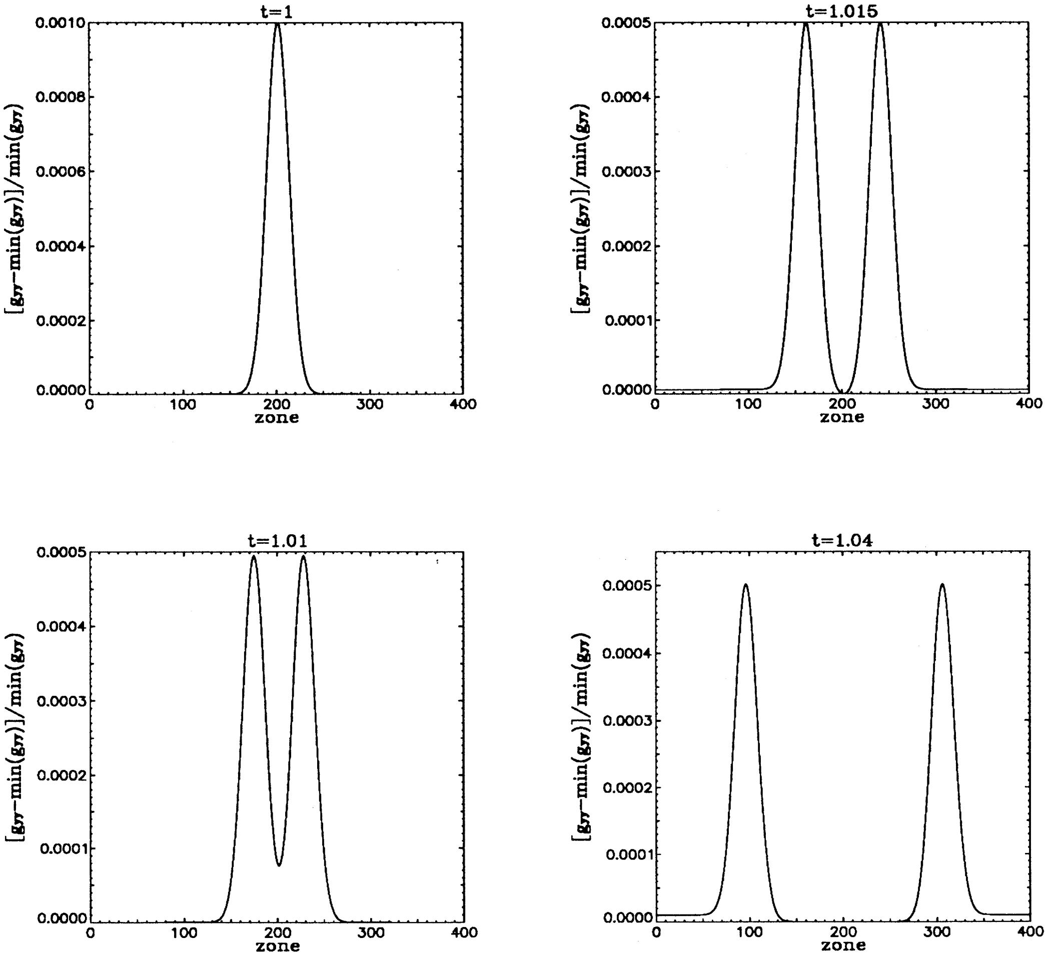

FIG. 7. Snapshots in time of solutions for the quantity (5.7) for the initial data (4.1) with $a=0.001$ and $L=0.05L_H$ at times $t=(1,1.01,1.015,1.04)$. The initial data in the form of a single pulse at $t=1$ splits into two oppositely directed traveling waves of smaller amplitude propagating outward toward the zone edges.

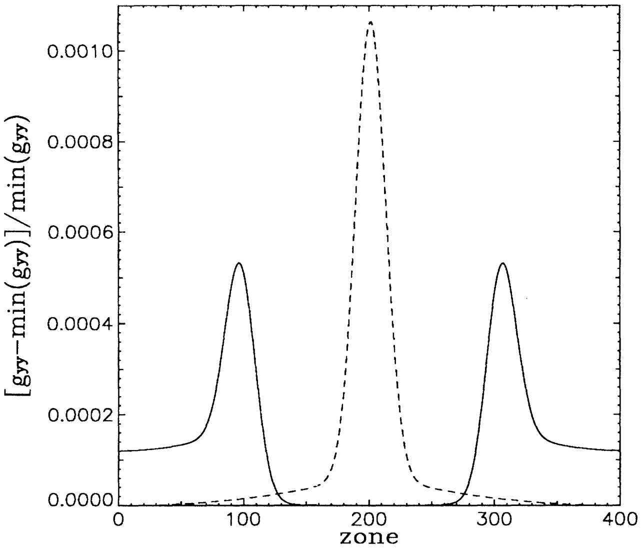

FIG. 8. Space profiles of the quantity (5.7) at time $t=1$ showing the initial data (dashed line) and at $t=2$ (solid line) for a moderate-frequency ($L=L_H$) Gaussian perturbation in the Kasner model of the form (4.1) with $a=0.001$. The waves are propagating outward toward the zone edges.

turbation and background are indistinguishable. In addition, the larger-amplitude case contributes to a larger averaged conformal factor and thereby increases the "energy" of the spacetime.

Results for perturbation lengths of order of the horizon size are similar to those in the high-frequency case. The nonlinear perturbation ($a=0.6$) interacts with and modifies the background spacetime, resulting in solutions quite different from the form of the free data. From Fig. 2 we see that the linear amplitude ($a=0.001$) which produced no visible effect in the high-frequency limit now produces a slight but noticeable distortion in the form of a less than exponential flattening of the pulse boundaries. This shows that small-amplitude perturbations may still act as non-negligible sources for background curvature if the characteristic perturbation length is not small compared to the horizon size.[14–16]

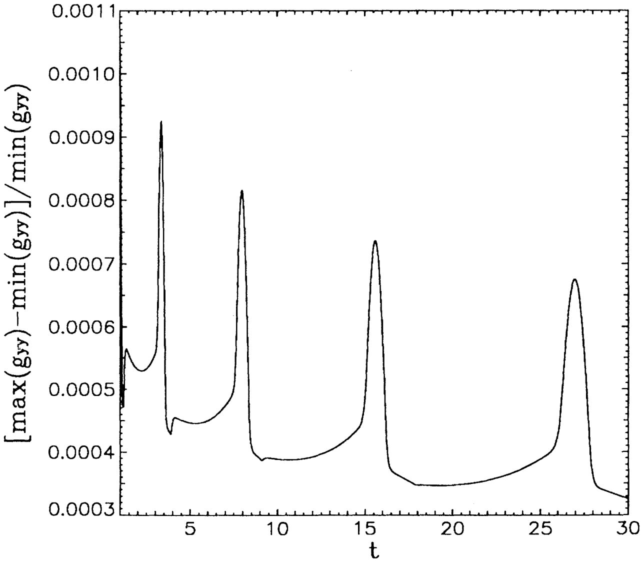

FIG. 9. Evolution of (5.1) for the same case as Fig. 8.

The large-amplitude solutions of Figs. 1 and 2 are qualitatively similar, differing only in their numerical scales. These nonlinear wave distortions were predicted from our analytical solution[2] for $\phi$ with pulse wave initial data. This solution was based on a particular form of a localized pulse in the free data which easily allowed a first-order analytic solution. In setting the free data, the grid was split into three parts. The center piece contained the wave pulse, while the two outer regions were set to the value of the flat-space background. The conformal factor $\phi$ had exponential solutions in the regions outside the wave pulse domain. These regions were distorted by the wave pulse and given a nonvanishing curvature similar to that shown in Figs. 1 and 2 as a result of satisfying the continuity conditions for $\phi$ and $\phi'$ across the different regions along the grid.

The local Bel-Robinson velocity field shown in Fig. 3 for the case $L=L_H$ indicates that there exist fluxes of energy moving in opposite directions symmetrically. The small-amplitude case shows that only the portion of the grid containing the perturbation has a velocity field in the positive and negative $z$ directions. The distinction between the pulse and background is clear, indicating that our data set is a superposition of two wave pulses which propagate in opposite directions along the $z$ axis. In the nonlinear case one cannot separate the pulse from the background; the entire grid has a nonvanishing Bel-Robinson velocity field. We will discuss this velocity further in the next section when we consider the propagation of these wave pulses.

These solutions may also be characterized by the Newman-Penrose scalars $\Psi_0$ and $\Psi_4$, which represent, respectively, the leftward, and rightward-propagating pieces of the Riemann tensor. We display $\Psi_0$ and $\Psi_4$ in Fig. 4. Note that apart from an overall scale factor, the profiles of $\Psi_0$ and $\Psi_4$ in the small- and large-amplitude cases are similar. However, the Coulomb part $\Psi_2$ displayed in Fig. 4 shows a marked difference in the linear and nonlinear regimes. The traveling gravitational waves are dominantly linear in the initial-value construction, and the nonlinearity of the Einstein equations is confined to the nonradiative or Coulomb part of the initial data. This behavior is expected since the momentum constraint is linear in $\hat{A}$, while the Hamiltonian constraint is nonlinear in $\phi$.

## V. EVOLUTION OF PULSE WAVE INITIAL DATA

In this section we evolve the pulselike initial data presented above for the case $L=0.05L_H$ and $a=0.001$. For all the simulations discussed here, we found it necessary to use 400 zones to achieve sufficient resolution to suppress numerical dispersion.[3] As expected from the previous section, this initial data set consists of two oppositely traveling waves superimposed on the grid center at $t=1$. They then separate and travel across the grid in opposite directions. The periodic boundary conditions wrap the spatial grid to connect and match $z=0$ with $z=L$, producing a toroidal geometry. As a result, when a wave reaches the grid boundary, it reemerges on the opposite side traveling in the same direction.

We characterize the evolution of the metric component $g_{yy}$ by plotting the quantity

$$\frac{\max_{\rm grid}(g_{yy})-\min_{\rm grid}(g_{yy})}{\min_{\rm grid}(g_{yy})}\,, \tag{5.1}$$

with a solid line, in Fig. 5. The amplitudes of the large spikes, which represent moments of collision of the pulses, are twice the amplitude of the individual peaks described by the regions between the spikes. This indicates that the wave pulses are behaving in a linear manner during the collision since their combined amplitude during the interaction period is a linear superposition of their individual peaks. The dashed lines of Fig. 5 are plots of the function $bt^{-1/6}$ where $b=a$ for the top curve and $b=a/2$ for the bottom showing that the peak amplitudes decay as $t^{-1/6}$ as predicted from our first-order high-frequency wave solutions for the Kasner model.[3]

Note also that the distance between the spikes in Fig. 5 is gradually increasing, indicating that the coordinate velocity of the wave peaks is decreasing. This behavior is predicted by our analytic solutions (3.4) and (3.5) describing the propagation of small-amplitude high-frequency monochromatic traveling waves. We showed that our metric variables are given by solutions of the form

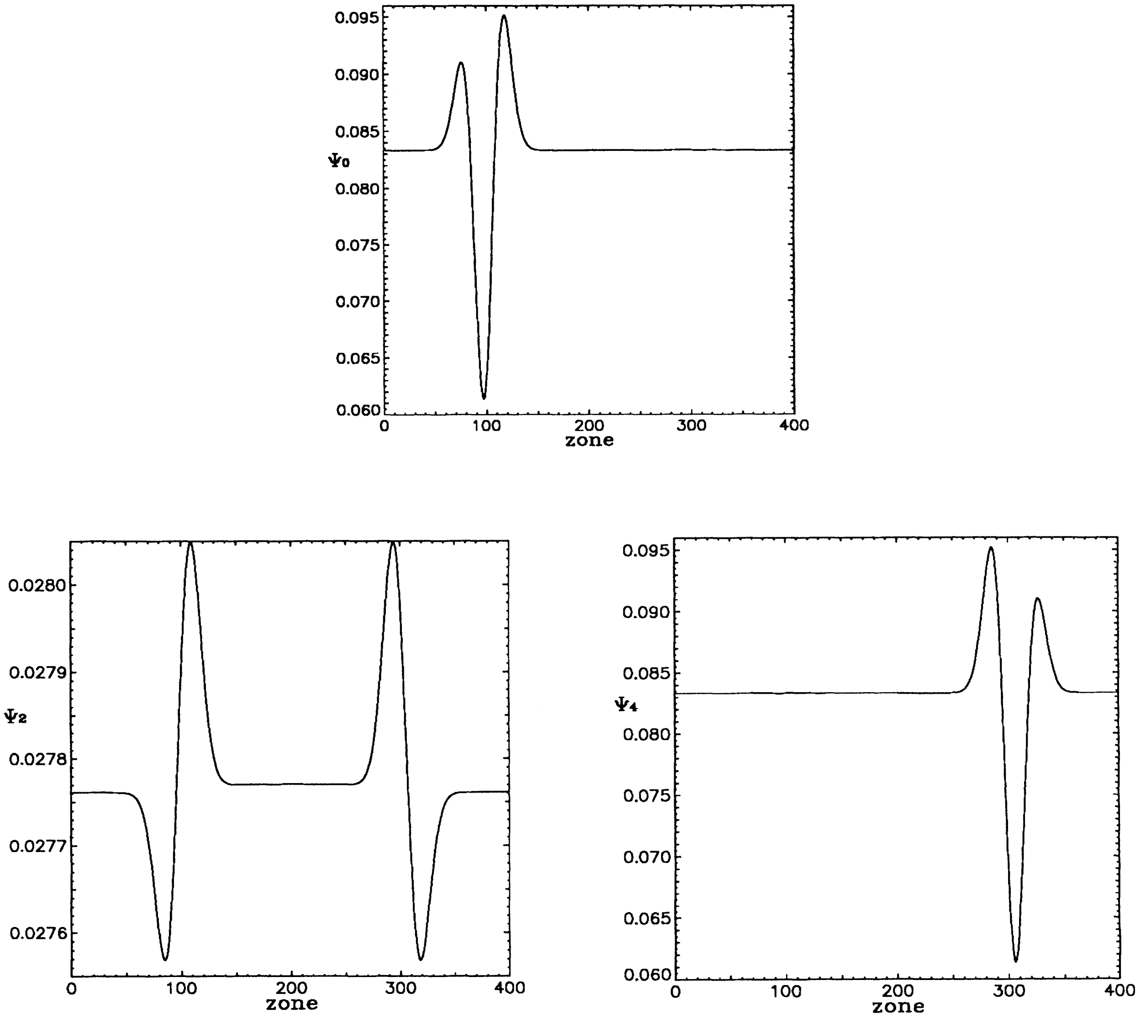

FIG. 10. Newman-Penrose scalars $\Psi_0$, $\Psi_2$, and $\Psi_4$ for the case of small-amplitude ($a=0.001$) perturbations with $L=L_H$ at time $t=2$ when the two pulses are well separated in space. These graphs are to be compared with Fig. 4 where we plot the corresponding initial data at $t=1$.

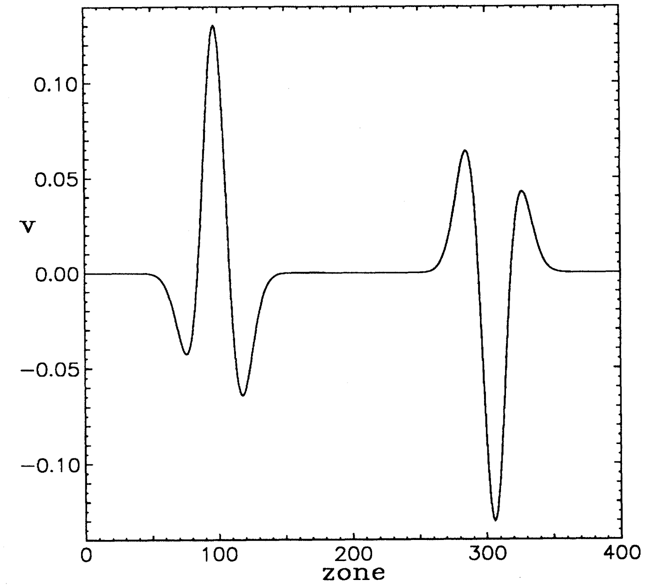

FIG. 11. Bel-Robinson velocity ($v$) at $t=2$ for the same moderate-frequency small-amplitude case as Fig. 10.

$$\chi=\chi(t)e^{i(kz\pm 3kt^{1/3})}, \tag{5.2}$$

where $\chi$ denotes any metric or momentum variable and the time-dependent amplitude $\chi(t)$ is a power-law denoting wave decay. The wave part of (5.2) is described by the oscillating piece whose phase we denote by $\theta=kz\pm 3k^{1/3}$. For an arbitrary phase $\theta(z,t)$, we can define[17] the local wave number

$$\kappa(z,t)=\frac{\partial\theta}{\partial z}=k \tag{5.3}$$

and local frequency

$$\omega(z,t)=\frac{\partial\theta}{\partial t}=W(\kappa)=kt^{-2/3}, \tag{5.4}$$

where $W(\kappa)$ is the dispersion relation. From these equations we find that the phase and group velocities are the same and equal to $t^{-2/3}$. We note that this is also the coordinate velocity for photons propagating in the homogeneous Kasner model, indicating that wave pulses are traveling along null lines to first order. This result suggests that any group of linear waves, such as small-amplitude pulses, will propagate with a time-dependent coordinate velocity $C(t)=t^{-2/3}$ across the grid.

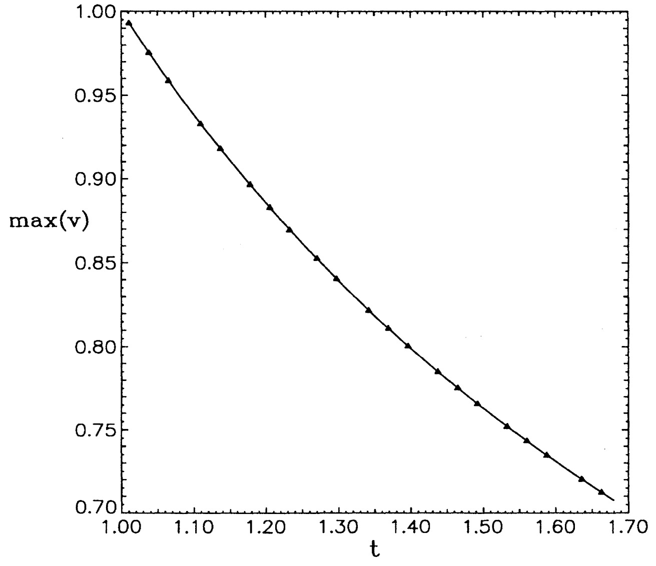

FIG. 12. Evolution of the maximum value of the Bel-Robinson velocity ($v$) across the grid. Triangles represent the code results, and the solid line is the analytic expression for the group velocity ($=t^{-2/3}$).

We now show that the group velocity produced by the code agrees with this analytical expression. Figure 6 plots the analytic solution with a solid line and the code results with triangles. The computed results were obtained by tracking the world lines of a single peak and making the assumption that the peak moves with uniform velocity between collisions (this assumption is not strictly valid and is responsible for the slight discrepancies between theory and computation in Fig. 6). Velocities were calculated between moments of collision by

$$C(t^{n+1/2})_{\text{code}}=\frac{\Delta z}{\Delta t}=\frac{L/2}{t^{n+1}-t^{n}}, \tag{5.5}$$

where $L/2$ is the distance between collisions which occur at the grid center and edges at time $t^{n}$ and $t^{n+1}$ (the integer $n$ denotes the $n$th collision).

The flat-space perturbations have solutions of the form

$$\chi=\chi(t)e^{i(kz\pm kt)}, \tag{5.6}$$

which has the linear time-independent dispersion relation $\omega=k$. Linear wave pulses in flat space travel at a uniform coordinate velocity equal to the coordinate speed of light in that model (unity in our geometric units). We have verified that this behavior holds in the numerical simulations as well.

Another property observed in Fig. 5 is the slight dip in the plotted quantity (5.1) immediately following the large spikes representing the interaction region. To understand this behavior, Fig. 7 presents snapshots of the space profile for

$$\frac{g_{yy}(z)-\min_{\text{grid}}(g_{yy})}{\min_{\text{grid}}(g_{yy})}, \tag{5.7}$$

at times $t=(1,1.01,1.015,1.04)$ for $L=0.05L_H$ and $a=0.001$. These results show the initial data in the form of a single pulse at $t=1$ splitting into two oppositely directly traveling waves of smaller amplitude. When the waves separate they leave in their wake a flat region which is of a different and lower value than the background regions in front of the pulses. This behavior was also noticed by Ove[18] who has studied similar initial data. The difference between the smooth regions before and after the wave front diminishes with time. This is attributed to the expansion of the Universe and the growth of the horizon size which together decrease the ratio $L/L_H$, resulting in more linear behavior. The metric component $g_{xx}$ also displays this type of behavior (see Fig. 8 to be discussed below).

The difference between the smooth regions in front of and behind the wave pulses is sensitive to the size of the characteristic perturbation length relative to the horizon size. To verify this we evolved small-amplitude ($a=0.001$) initial data identical to the previous case except with $L=L_H$. We plot the quantity (5.7) in Fig. 8. Dashed lines refer to the initial data at $t=1$ and the solid lines to $t=2$. This figure is to be compared with Fig. 7 for which $L=0.05L_H$. The high-frequency small-amplitude pulses in Fig. 7 behave more like linear traveling waves. The propagation of lower-frequency waves affect the background regions of spacetime more visibly as seen in Fig. 8.

We also present, in Fig. 9, the evolution of the quantity (5.1) for the case $L=L_H$, which shows very noticeable dips following the large spikes at early times. Initially, differences in the background spacetimes following and preceding the wave fronts are large. However, these differences diminish dramatically in time as the waves decay and the cosmology expands and $L$ becomes smaller than the horizon size $L_H$.

We present profiles of the Newman-Penrose scalars and Bel-Robinson velocity in Figs. 10 and 11 for the case of small-amplitude perturbations with $L=L_H$ at time $t=2$ when the two pulses are well separated in space. These graphs are to be compared with Fig. 4 where we have plotted the corresponding initial-value quantities at $t=1$. Note that the space profiles of $\Psi_0$ and $\Psi_4$ describing the individual pulses at $t=2$ may be superimposed on the corresponding profiles at the initial time $t=1$ to yield

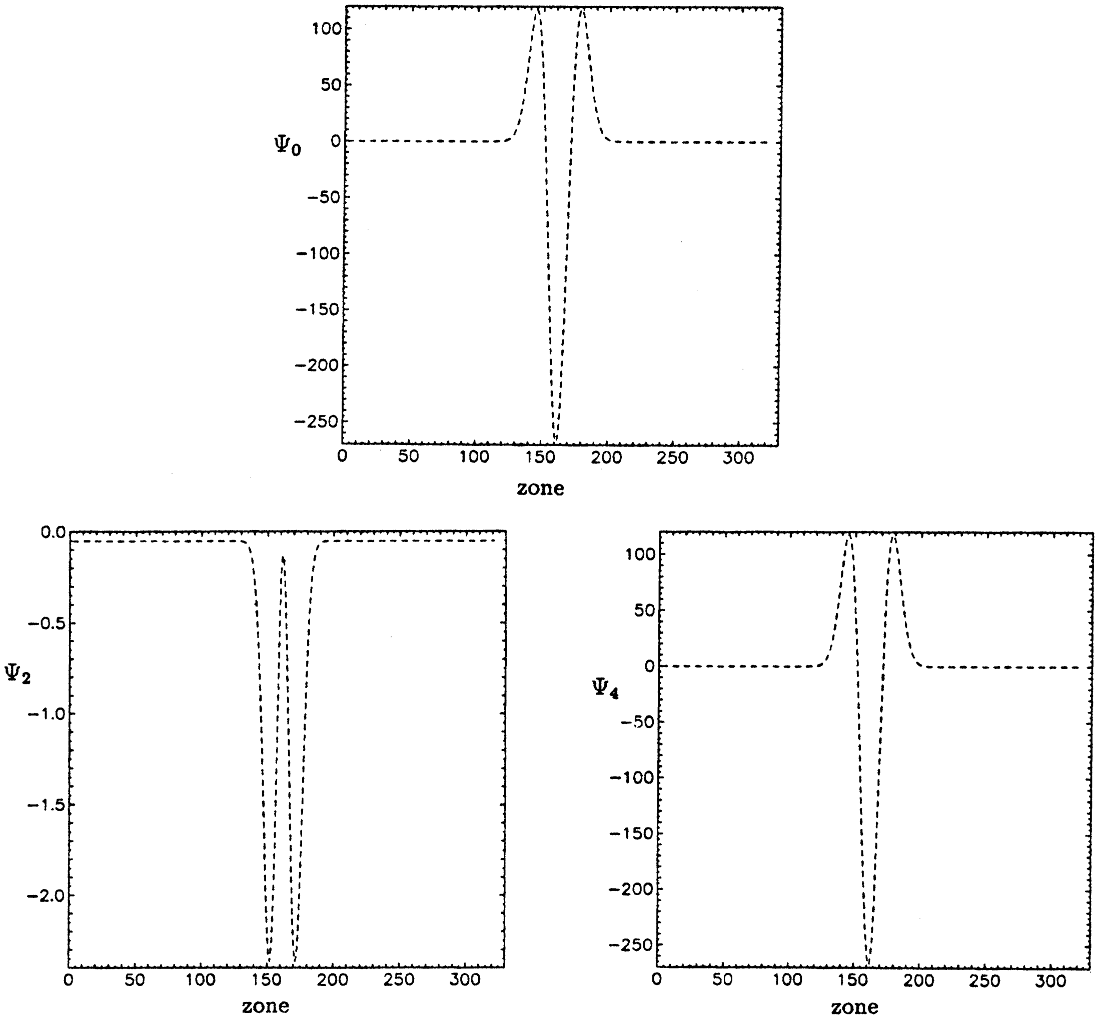

FIG. 13. Newman-Penrose scalars $\Psi_0$, $\Psi_2$, and $\Psi_4$ for the initial data in the case of large-amplitude ($a=0.1$) perturbations with $L=0.05L_H$.

qualitatively the same shapes. They differ only by an overall scale factor attributed to the cosmological expansion and evidenced in the conformal factor. We also note that $\Psi_2$ exhibits a difference in background values on either side of the wave fronts. This suggests that the two traveling wave pulses interact linearly while the Coulomb part $\Psi_2$ behaves nonlinearly as we observed in the previous section.

In addition, we find from Fig. 11 that the velocity $v$ defined by the ratio of superenergy to flux is a useful quantity in tracking our wave solutions. We present a plot of the maximum value of $v$ across the grid versus time in Fig. 12. Triangles represent the code solutions for the value of $v$ at the peak, and a solid line graphs the analytic expression of the group velocity $=t^{-2/3}$. The peak of the Bel-Robinson velocity across the grid is equal to the coordinate speed of light and is thus a measure of the wave propagation speed for a pulse as it travels along the $z$ axis.

Finally, we mention that our work included large-amplitude ($a=0.1-0.5$) pulse waves with high ($L=0.05L_H$) to moderate ($L=L_H$) frequencies. Our results for these cases are qualitatively similiar to the smaller-amplitude ($a=0.001$) cases with the corresponding frequencies. Figure 13 shows the Newman-Penrose scalars for the initial data (4.1) with $a=0.1$, $w=0.03$, and $L=0.05L_H$, and Fig. 14 displays their profiles at a later time when the two pulses are well separated in space. One can see that the propagating pieces $\Psi_0$ and $\Psi_4$ display no evidence of any nonlinear interaction, while the nonradiative component $\Psi_2$ is visibly altered as the wave pulses separate. The wave pulses distort the spacetime through which they propagate in a more complicated fashion than the corresponding small-amplitude case in addition to affecting the level of the smooth or background regions through which they travel.

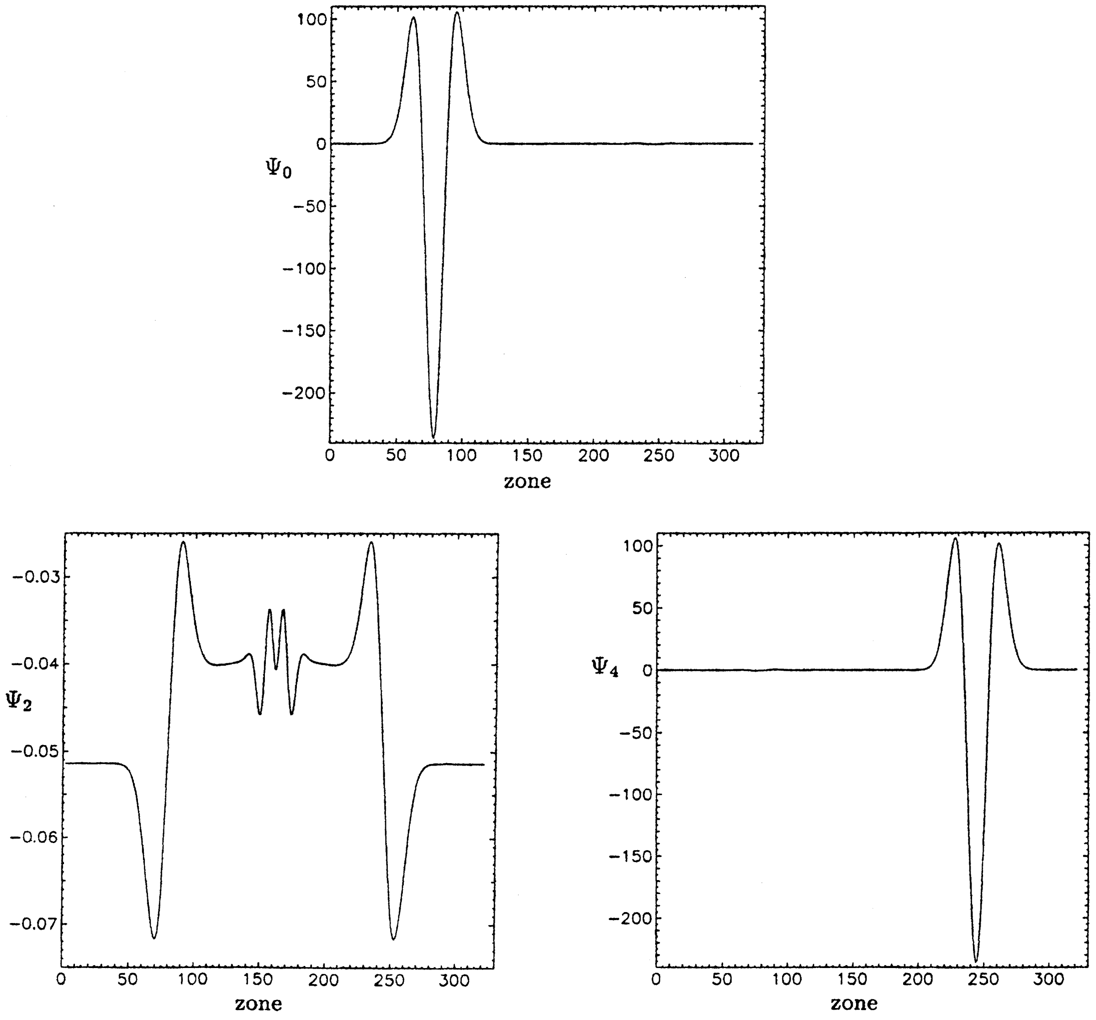

FIG. 14. As in Fig. 13, except here $\Psi_0$, $\Psi_2$, and $\Psi_4$ are displayed at a later time when the pulses are well separated in space.

## VI. CONCLUSIONS

We have presented linear and nonlinear solutions for "wave packet" free data to the Einstein equations in an expanding Kasner cosmology. Although we have not presented graphical illustrations of flat-space perturbations in this paper, we note that they possess the same qualitative features as the Kasner perturbations. To aid in understanding the numerical solutions, we computed a number of diagonstic quantities, including the Newman-Penrose scalars and the Bel-Robinson velocity, both of which provide useful characterizations of wave properties.

We found that both the perturbation amplitude $a$ and the ratio $L/L_H$ of perturbation length to horizon size are important parameters. The linear high-frequency regime is the limit of $a$, $L/L_H \ll 1$. In this limit solutions to the initial-value equations reproduce the localized nature of the free data, and one has the picture of a distinct wave pulse propagating on an otherwise undisturbed background spacetime. In the nonlinear regime $a$, $L/L_H \sim 1$, "perturbation" and background are indistinguishable in the metric components. Our results indicate that our perturbative analysis breaks down at $a$, $L/L_H \sim 0.05$, where nonlinear behavior is clearly evident (see, for example, Fig. 7) and not modeled by our analytic methods.

For the small-amplitude $(a=0.001)$ moderate-wavelength $(L=L_H)$ case, we found a dominantly linear wave behavior, since the shapes of the two waves before, during, and after their interaction are qualitatively the same. The nonlinearity shows up in the single Newman-Penrose scalar $\Psi_2$, which exhibits very different profiles when the two peaks are separated and when they are interacting. Furthermore, large length scale perturbations have the peculiar property that background regions in front of and behind the waves are different. This behavior is evident in our plots of $\Psi_2$. It appears that the nonlinearity of the Einstein equations is evidenced in the nonradiative of Coulomb part of the curvature tensor $R_{\alpha\beta\gamma\delta}$.

To lowest order linear high-frequency waves travel without dispersing ($\omega=k$ for flat space and $\omega=kt^{-2/3}$ for the Kasner model) along null lines with coordinate velocities equal to the velocity of light. We presented numerical evidence of this through the computation of the Bel-Robinson velocity and the tracking of the world lines of the wave peaks. While we have not obtained a dispersion relation to second order, we were able to derive some analytic results in the nonlinear regime. Our analytic second-order solution shows that a first-order standing wave produces a homogeneous oscillation with frequency equal to the second-harmonic frequency of the linear wave and increases the expansion rate. The detection of wave dispersion is complicated by artificially induced numerical dispersion attributed to finite differencing. However, we have demonstrated[3] that numerical dispersion for our case vanishes with higher resolution as $\sim(\Delta z)^2$ and is therefore a controllable problem and not significant in the cases presented here. We have found no numerical evidence of sufficiently well zoned waves dispersing, nor have we found any tendency of waves to steepen and shock. Wave pulses propagate essentially linearly.

We have also evolved large-amplitude waves in the moderate- and high-frequency regimes for both the flat and Kasner backgrounds. The results in those cases proved similar to the small amplitude moderate-frequency perturbations which showed a dominantly linear wave propagation. Nonlinear behavior was found only in the Coulomb field.

## ACKNOWLEDGMENTS

We are pleased to acknowledge stimulating discussions with J. W. York. Computations reported here were carried out at the National Center for Supercomputing Applications (University of Illinois). This work was supported by NSF Grants Nos. PHY-8451732, PHY-8706315, PHY-8404931, and PHY-8806567, and by Cray Research, Inc.

## APPENDIX

In this appendix we present results for all geometrical quantities necessary to describe our three-metric defined by (1.1) as

$$\gamma_{ij}=\phi^4\begin{bmatrix}1 & 0 & 0\\ 0 & h^2 & 0\\ 0 & 0 & 1\end{bmatrix} . \tag{A1}$$

The nonvanishing Christoffel symbols for the metric (A1) are

$$\begin{aligned}&\Gamma^3_{11}=-2\frac{\phi'}{\phi},\quad \Gamma^2_{23}=2\frac{\phi'}{\phi}+\frac{h'}{h} ,\\ &\Gamma^1_{13}=2\frac{\phi'}{\phi},\quad \Gamma^3_{33}=2\frac{\phi'}{\phi} ,\\ &\Gamma^3_{22}=-2h^2\frac{\phi'}{\phi}-hh' ,\end{aligned} \tag{A2}$$

where primes refer to differentiation with respect to the coordinate $z$. Using these, we derive the components of the Ricci tensor:

$$\begin{aligned}&R_{11}=-2\frac{\phi''}{\phi}-2\frac{(\phi')^2}{\phi^2}-2\frac{h'}{h}\frac{\phi'}{\phi} ,\\ &R_{22}=-2\frac{\phi''h^2}{\phi}-2\frac{(\phi'h)^2}{\phi^2}-4\frac{hh'\phi'}{\phi}-hh'' ,\\ &R_{33}=-4\frac{\phi''}{\phi}+4\frac{(\phi')^2}{\phi^2}-2\frac{h'}{h}\frac{\phi'}{\phi}-\frac{h''}{h} ,\end{aligned} \tag{A3}$$

and the corresponding scalar curvature

$$R=-8\frac{\phi''}{\phi^5}-8\frac{h'\phi'}{h\phi^5}-2\frac{h''}{h\phi^4} . \tag{A4}$$

We have found it convenient to decompose the vacuum four-dimensional Riemann tensor $R_{\alpha\beta\gamma\delta}$ into its "electric" $E_{\alpha\beta}$ and "magnetic" $B_{\alpha\beta}$ parts[10,12] as

$$\begin{aligned}R_{\alpha\beta\gamma\delta}=&\,n_\alpha n_\delta E_{\beta\gamma}-n_\alpha n_\gamma E_{\beta\delta}-n_\beta n_\delta E_{\alpha\gamma}\\ &+n_\beta n_\gamma E_{\alpha\delta}+n_\alpha\epsilon_{\mu\gamma\delta}B^\mu_\beta-n_\beta\epsilon_{\mu\gamma\delta}B^\mu_\alpha\\ &+n_\gamma\epsilon_{\mu\alpha\beta}B^\mu_\delta-n_\delta\epsilon_{\mu\alpha\beta}B^\mu_\gamma+\epsilon_{\alpha\beta\mu}E^{\mu\nu}\epsilon_{\nu\gamma\delta} ,\end{aligned} \tag{A5}$$

where

$$E_{\alpha\beta}=n^{\gamma}R_{\gamma\alpha\beta\delta}n^{\delta}\ , \tag{A6}$$

$$B_{\alpha\beta}=\tfrac{1}{2}\epsilon_{\alpha}^{\gamma\mu}n^{\lambda}\gamma_{\beta}^{\nu}R_{\lambda\nu\gamma\mu}\ , \tag{A7}$$

with $\epsilon_{\alpha}^{\gamma\mu}=\epsilon^{\gamma\mu}{}_{\alpha\beta}n^{\beta}$ and $\gamma_{\beta}^{\nu}=g_{\beta}^{\nu}+n^{\nu}n_{\beta}$, where $g_{\alpha\beta}$ is the full four-dimensional spacetime metric defined by (1.1). The unit normal vector field to a given time slice is denoted by $n^{\alpha}$ and $\epsilon^{\alpha\beta\gamma\delta}$ is the completely antisymmetric Levi-Civita tensor density. The tensors $E_{\alpha\beta}$ and $B_{\alpha\beta}$ are useful because they can be constructed from our local three-metric $\gamma_{\alpha\beta}$ and the extrinsic curvature tensor[10,12] as

$$E_{ij}=-R_{ij}-KK_{ij}+K_{im}K_{j}^{m}\ , \tag{A8}$$

$$B_{ij}=\gamma_{il}\gamma_{jk}\epsilon^{lmn}D_{n}K_{m}^{k}\ , \tag{A9}$$

where Latin indices denote spatial components and $E_{0\beta}=B_{0\beta}=0$. The nonzero components for our three-metric (A1) are written as

$$\begin{aligned}
\frac{E_{11}}{\gamma_{11}}&=(K^{1}{}_{1})^{2}-KK^{1}{}_{1}-\frac{R_{11}}{\gamma_{11}}\ ,\\
\frac{E_{22}}{\gamma_{22}}&=(K^{2}{}_{2})^{2}-KK^{2}{}_{2}-\frac{R_{22}}{\gamma_{22}}\ ,\\
\frac{E_{33}}{\gamma_{33}}&=(K^{3}{}_{3})^{2}-KK^{3}{}_{3}-\frac{R_{33}}{\gamma_{33}}\ ,
\end{aligned} \tag{A10}$$

and

$$\frac{B_{12}}{\sqrt{\gamma_{11}\gamma_{22}}}=\frac{1}{\sqrt{\gamma_{33}}}(K^{2}{}_{2,3}+\Gamma_{23}^{2}K^{2}{}_{2}-\Gamma_{23}^{2}+K^{3}{}_{3})\ . \tag{A11}$$

The Newman-Penrose scalars are written in terms of $E_{\alpha\beta}$ and $B_{\alpha\beta}$ as

$$\begin{aligned}
\Psi_{0}&=\frac{1}{2}\left[\frac{E_{22}}{\gamma_{22}}-\frac{E_{11}}{\gamma_{11}}\right]-\frac{B_{12}}{\sqrt{\gamma_{11}\gamma_{22}}}\ ,\\
\Psi_{4}&=\frac{1}{2}\left[\frac{E_{22}}{\gamma_{22}}-\frac{E_{11}}{\gamma_{11}}\right]+\frac{B_{12}}{\sqrt{\gamma_{11}\gamma_{22}}}\ ,\\
\Psi_{2}&=-\frac{1}{2}\left[\frac{E_{33}}{\gamma_{33}}\right]\ ,
\end{aligned} \tag{A12}$$

and the Bel-Robinson variables as

$$\begin{aligned}
p^{1}&=p^{2}=0\ ,\\
p^{3}&=\frac{B_{12}}{\sqrt{\gamma}}\left[\frac{E_{22}}{\gamma_{22}}-\frac{E_{11}}{\gamma_{11}}\right]\ ,\\
E_{s}&=\frac{1}{2}\left[\left[\frac{E_{11}}{\gamma_{11}}\right]^{2}+\left[\frac{E_{22}}{\gamma_{22}}\right]^{2}+\left[\frac{E_{33}}{\gamma_{33}}\right]^{2}\right]+\frac{(B_{12})^{2}}{\gamma_{11}\gamma_{22}}\ ,
\end{aligned} \tag{A13}$$

where $\gamma$ is the determinant of (A1).

---

[*] Present address: Department of Physics and Center for Relativity, The University of Texas at Austin, Austin, TX 78712.

[1] P. Anninos, J. Centrella, and R. Matzner, Phys. Rev. D **39**, 2155 (1989).

[2] P. Anninos, J. Centrella, and R. Matzner, in *Frontiers of Numerical Relativity,* edited by C. Evans, L. S. Finn, and D. Hobill (Cambridge University Press, Cambridge, England, 1989), p. 342.

[3] P. Anninos, J. Centrella, and R. Matzner, preceding paper, Phys. Rev. D **43**, 1808 (1991).

[4] B. Berger, Ann. Phys. (N.Y.) **83**, 458 (1974).

[5] R. Gowdy, Phys. Rev. Lett. **27**, 826 (1971).

[6] R. Gowdy, Ann. Phys. (N.Y.) **83**, 203 (1974).

[7] E. Newman and R. Penrose, J. Math. Phys. **3**, 566 (1962).

[8] J. W. York (private communication).

[9] P. Szekeres, J. Math. Phys. **6**, 1387 (1965).

[10] L. L. Smarr, in *Eighth Texas Symposium on Relativistic Astrophysics,* edited by M. D. Papagiannis (Annals of the Academy of Sciences, New York, 1977), Vol. 302, p. 569.

[11] V. D. Zakharov, *Gravitational Waves in Einstein's Theory* (Halsted, Jersuselm, 1973).

[12] L. L. Smarr, Ph.D. thesis, University of Texas at Austin, 1975.

[13] M. Abramowitz and I. A. Stegun, *Handbook of Mathematical Functions* (Dover, New York, 1972).

[14] R. A. Isaacson, Phys. Rev. **166**, 1263 (1968).

[15] R. A. Isaacson, Phys. Rev. **166**, 1272 (1968).

[16] K. S. Thorne, in *Nonlinear Phenomena in Physics,* edited by F. Claro (Springer, New York, 1985), p. 280.

[17] G. B. Whitham, *Linear and Nonlinear Waves* (Wiley, New York, 1974).

[18] R. Ove, Phys. Rev. Lett. **64**, 1200 (1990).